Superconducting series nanowire detector counting up to twelve photons

Document status and date:
Published: 01/01/2014

Document Version:
Publisher's PDF, also known as Version of Record (includes final page, issue and volume numbers)

Please check the document version of this publication:

• A submitted manuscript is the version of the article upon submission and before peer-review. There can be important differences between the submitted version and the official published version of record. People interested in the research are advised to contact the author for the final version of the publication, or visit the DOI to the publisher's website.
• The final author version and the galley proof are versions of the publication after peer review.
• The final published version features the final layout of the paper including the volume, issue and page numbers.

Link to publication

Download date: 04. Oct. 2023

Superconducting series nanowire detector counting up to twelve photons

Zili Zhou,[1,*] Saeedeh Jahanmirinejad,[1] Francesco Mattioli,[2] Döndü Sahin,[1] Giulia Frucci,[1] Alessandro Gaggero,[2] Roberto Leoni,[2] and Andrea Fiore[1]

[1] *COBRA Research Institute, Eindhoven University of Technology, PO Box 513, 5600 MB Eindhoven, The Netherlands*
[2] *Istituto di Fotonica e Nanotecnologie, CNR, Via Cineto Romano 42, 00156 Roma, Italy*
[*]z.zhou@tue.nl

Abstract: We demonstrate a superconducting photon-number-resolving detector capable of resolving up to twelve photons at telecommunication wavelengths. It is based on a series array of twelve superconducting NbN nanowire elements, each connected in parallel with an integrated resistor. The photon-induced voltage signals from the twelve elements are summed up into a single readout pulse with a height proportional to the detected photon number. Thirteen distinct output levels corresponding to the detection of n = 0-12 photons are observed experimentally. A detailed analysis of the linearity and of the excess noise shows the potential of scaling to an even larger dynamic range.

References and links

1. E. Knill, R. Laflamme, and G. J. Milburn, "A scheme for efficient quantum computation with linear optics," Nature **409**(6816), 46–52 (2001).
2. N. Sangouard, C. Simon, J. Minář, H. Zbinden, H. de Riedmatten, and N. Gisin, "Long-distance entanglement distribution with single-photon sources," Phys. Rev. A **76**(5), 050301 (2007).
3. A. E. Lita, A. J. Miller, and S. W. Nam, "Counting near-infrared single-photons with 95% efficiency," Opt. Express **16**(5), 3032–3040 (2008).
4. M. Fujiwara and M. Sasaki, "Direct measurement of photon number statistics at telecom wavelengths using a charge integration photon detector," Appl. Opt. **46**(16), 3069–3074 (2007).
5. M. J. Fitch, B. C. Jacobs, T. B. Pittman, and J. D. Franson, "Photon-number resolution using time-multiplexed single-photon detectors," Phys. Rev. A **68**(4), 043814 (2003).
6. L. A. Jiang, E. A. Dauler, and J. T. Chang, "Photon-number-resolving detector with 10 bits of resolution," Phys. Rev. A **75**(6), 062325 (2007).
7. D. A. Kalashnikov, S. H. Tan, and L. A. Krivitsky, "Crosstalk calibration of multi-pixel photon counters using coherent states," Opt. Express **20**(5), 5044–5051 (2012).
8. M. Ramilli, A. Allevi, V. Chmill, M. Bondani, M. Caccia, and A. Andreoni, "Photon-number statistics with silicon photomultipliers," J. Opt. Soc. Am. B **27**(5), 852–862 (2010).
9. E. Waks, K. Inoue, W. D. Oliver, E. Diamanti, and Y. Yamamoto, "High-efficiency photon-number detection for quantum information processing," IEEE J. Sel. Top. Quantum Electron. **9**(6), 1502–1511 (2003).
10. B. E. Kardynał, Z. L. Yuan, and A. J. Shields, "An avalanche-photodiode-based photon-number-resolving detector," Nat. Photonics **2**(7), 425–428 (2008).
11. G. Gol'tsman, O. Okunev, G. Chulkova, A. Lipatov, A. Semenov, K. Smirnov, B. Voronov, A. Dzardanov, C. Williams, and R. Sobolewski, "Picosecond superconducting single-photon optical detector," Appl. Phys. Lett. **79**(6), 705 (2001).
12. F. Marsili, V. Verma, J. Stern, S. Harrington, A. Lita, T. Gerrits, I. Vayshenker, B. Baek, M. Shaw, R. Mirin, and S. W. Nam, "Detecting single infrared photons with 93% system efficiency," Nat. Photonics **7**(3), 210–214 (2013).
13. D. Bitauld, F. Marsili, A. Gaggero, F. Mattioli, R. Leoni, S. J. Nejad, F. Lévy, and A. Fiore, "Nanoscale optical detector with single-photon and multiphoton sensitivity," Nano Lett. **10**(8), 2977–2981 (2010).
14. Z. Zhou, G. Frucci, F. Mattioli, A. Gaggero, R. Leoni, S. Jahanmirinejad, T. B. Hoang, and A. Fiore, "Ultrasensitive *N*-photon interferometric autocorrelator," Phys. Rev. Lett. **110**(13), 133605 (2013).
15. J. J. Renema, G. Frucci, Z. Zhou, F. Mattioli, A. Gaggero, R. Leoni, M. J. A. de Dood, A. Fiore, and M. P. van Exter, "Modified detector tomography technique applied to a superconducting multiphoton nanodetector," Opt. Express **20**(3), 2806–2813 (2012).

16. M. Bell, A. Antipov, B. Karasik, A. Sergeev, V. Mitin, and A. Verevkin, "Photon number-resolved detection with sequentially connected nanowires," IEEE Trans. Appl. Supercond. **17**(2), 289–292 (2007).
17. J. Kitaygorsky, S. Dorenbos, E. Reiger, R. Schouten, V. Zwiller, and R. Sobolewski, "HEMT-based readout technique for dark- and photon-count studies in NbN superconducting single-photon detectors," IEEE Trans. Appl. Supercond. **19**(3), 346–349 (2009).
18. E. A. Dauler, B. S. Robinson, A. J. Kerman, J. K. W. Yang, K. M. Rosfjord, V. Anant, B. Voronov, G. Gol'tsman, and K. K. Berggren, "Multi-element superconducting nanowire single-photon detector," IEEE Trans Appl. Supercond. **17**(2), 279–284 (2007).
19. A. Divochiy, F. Marsili, D. Bitauld, A. Gaggero, R. Leoni, F. Mattioli, A. Korneev, V. Seleznev, N. Kaurova, O. Minaeva, G. Gol'tsman, K. G. Lagoudakis, M. Benkhaoul, F. Lévy, and A. Fiore, "Superconducting nanowire photon-number-resolving detector at telecommunication wavelengths," Nat. Photonics **2**(5), 302–306 (2008).
20. F. Marsili, D. Bitauld, A. Gaggero, S. Jahanmirinejad, R. Leoni, F. Mattioli, and A. Fiore, "Physics and application of photon number resolving detectors based on superconducting parallel nanowires," New J. Phys. **11**(4), 045022 (2009).
21. S. Jahanmirinejad and A. Fiore, "Proposal for a superconducting photon number resolving detector with large dynamic range," Opt. Express **20**(5), 5017–5028 (2012).
22. S. Jahanmirinejad, G. Frucci, F. Mattioli, D. Sahin, A. Gaggero, R. Leoni, and A. Fiore, "Photon-number resolving detector based on a series array of superconducting nanowires," Appl. Phys. Lett. **101**(7), 072602 (2012).
23. D. Sahin, A. Gaggero, Z. Zhou, S. Jahanmirinejad, F. Mattioli, R. Leoni, J. Beetz, M. Lermer, M. Kamp, S. Hofling, and A. Fiore, "Waveguide photon-number-resolving detectors for quantum photonic integrated circuits," Appl. Phys. Lett. **103**(11), 111116 (2013).
24. A. Gaggero, S. J. Nejad, F. Marsili, F. Mattioli, R. Leoni, D. Bitauld, D. Sahin, G. J. Hamhuis, R. Notzel, R. Sanjines, and A. Fiore, "Nanowire superconducting single-photon detectors on GaAs for integrated quantum photonic applications," Appl. Phys. Lett. **97**(15), 151108 (2010).
25. J. A. Arnaud, W. M. Hubbard, G. D. Mandeville, B. de la Clavière, E. A. Franke, and J. M. Franke, "Technique for fast measurement of Gaussian laser beam parameters," Appl. Opt. **10**(12), 2775–2776 (1971).
26. V. Anant, A. J. Kerman, E. A. Dauler, J. K. W. Yang, K. M. Rosfjord, and K. K. Berggren, "Optical properties of superconducting nanowire single-photon detectors," Opt. Express **16**(14), 10750–10761 (2008).
27. A. J. Kerman, E. A. Dauler, J. K. W. Yang, K. M. Rosfjord, V. Anant, K. K. Berggren, G. N. Gol'tsman, and B. M. Voronov, "Constriction-limited detection efficiency of superconducting nanowire single-photon detectors," Appl. Phys. Lett. **90**(10), 101110 (2007).
28. F. Mattioli, R. Leoni, A. Gaggero, M. G. Castellano, P. Carelli, F. Marsili, and A. Fiore, "Electrical characterization of superconducting single-photon detectors," J. Appl. Phys. **101**(5), 054302 (2007).
29. K. M. Rosfjord, J. K. W. Yang, E. A. Dauler, A. J. Kerman, V. Anant, B. M. Voronov, G. N. Gol'tsman, and K. K. Berggren, "Nanowire Single-photon detector with an integrated optical cavity and anti-reflection coating," Opt. Express **14**(2), 527–534 (2006).
30. J. K. W. Yang, A. J. Kerman, E. A. Dauler, V. Anant, K. M. Rosfjord, and K. K. Berggren, "Modeling the electrical and thermal response of superconducting nanowire single-photon detectors," IEEE Trans. Appl. Supercond. **17**(2), 581–585 (2007).
31. E. A. Dauler, A. J. Kerman, B. S. Robinson, J. K. W. Yang, B. Voronov, G. Gol'tsman, S. A. Hamilton, and K. K. Berggren, "Photon-number-resolution with sub-30-ps timing using multi-element superconducting nanowire single photon detectors," J. Mod. Opt. **56**(2–3), 364–373 (2009).
32. G. P. Agrawal, *Fiber-Optic Communication Systems*, 3rd ed. (Wiley, New York, 2002), Chap. 4.5.

1. Introduction

Photon-number-resolving (PNR) detectors have attracted a large interest in the last decade. They play a key role in many fields such as linear-optics quantum computing [1] and quantum communication [2]. Ultimately, a PNR detector with a large dynamic range would represent an ideal photon detector combining single-photon sensitivity with a linear response. However, making a PNR detector that meets the requirements of these applications is challenging. It should have high efficiency, high speed, low jitter, low noise, the sensitivity at telecommunication wavelengths and the ability of resolving photon numbers with a large dynamic range. None of the existing PNR detectors meet all of these standards. For instances, transition edge sensors [3], charge integrated photon detectors [4] and PNR detectors based on time-multiplexing [5] are limited by their poor timing properties, arrays of InGaAs single photon avalanche detectors (SPADs) [6, 7] and arrays of silicon photomultipliers [8] have high dark count rates (DCR), visible light photon counters [9] are not sensitive at telecommunication wavelengths, and InGaAs SPADs with self-differencing circuits have a limited PNR dynamic range [10]. Superconducting single photon detectors (SSPDs) [11] are well known for their leading performance in the photodetection at telecommunication

wavelengths, providing high quantum efficiency (QE), short response time, low timing jitter, and low DCR [12]. PNR detectors based on SSPDs will benefit from these advantages and are promising to outpace the other existing PNR techniques.

The SSPDs operated with the conventional readout scheme (using an amplifier chain with a 50 Ω input impedance) do not provide the PNR functionality. Indeed, since the resistance of the NbN nanowire after photon absorption (~10^3 Ω) is much larger than the load resistance (50 Ω), the absorption of more than one photon in the wire results in a readout pulse with nearly the same height as the one produced by the absorption of a single photon. Therefore the SSPDs give a binary response to the number of incident photons (either '0 photon' or '≥ 1 photon'). Lowering the bias current of the SSPD will bring it to the multi-photon detection regimes [11, 13–15]. In this mode, the SSPD operates as a threshold detector (responding to ≥ n photons) but not as a PNR detector. Integrating an SSPD with a high impedance pre-amplifier may in principle enable the SSPD to have the PNR functionality [16]. However, the PNR resolution with this method was limited due to the latching problems [17]. An alternative way is spatial multiplexing [18, 19]. In this case, a number of SSPD elements are arranged in an array and equally illuminated under the input light beam. Each element acts as a single-photon detector and their responses are read either separately [18] or together [19] in the output. The former technique, i.e. reading the responses from a number of SSPD elements separately, requires the same number of readout electronic sets. Therefore it is not scalable to large photon numbers due to the correspondingly increasing experimental complexity. In contrast, the latter approach, i.e. reading the responses from different elements summed up together as a single readout signal, can avoid this problem. In this case, the detected photon number is measured from the height of the single readout signal. As reported in [19], an array of six superconducting nanowire elements connected in parallel, named parallel nanowire detector (PND), was able to resolve up to four photons with a record PNR performance. However, the PND has a drawback of current redistribution problems due to its parallel design. The bias current from the firing elements is partially redirected to the unfiring elements. This phenomenon introduces false photon detections and consequently limits the dynamic range [20]. In order to solve this problem, Jahanmirinejad *et al.* [21] proposed a novel design of a series connection of *N* superconducting nanowires named *series nanowire detector* (SND), which solves the current redistribution problem and is in principle scalable to large photon numbers. The first experimental demonstration of the SND, as a proof of principle, was reported in [22] with four elements (namely 4-SND), capable of resolving up to four photons. A waveguide-coupled 4-SND has also been demonstrated recently [23]. However, so far, the scalability of the SND to large photon numbers has not been proved experimentally. The excess noise observed in the 4-SNDs potentially represents a threat to the scalability, as it may undermine the discrimination between photon levels at large photon numbers.

In this work, we extend the PNR dynamic range of the SND to twelve photons. The SND presented here, named as 12-SND, is based on a series array of twelve superconducting NbN nanowire elements. The photon-induced voltage pulses produced by the switching elements are summed up into a single readout pulse with a height proportional to the number of firing elements and thus to the number of detected photons. Thirteen distinct output levels corresponding to the detection of n = 0-12 photons were obtained in the measurement, representing a record dynamic range for the fast PNR detectors at telecommunication wavelengths. The device quantum efficiency and the temporal properties of the device were characterized. Photon statistics were performed on the experimental data and shows a good agreement with the theory. A detailed analysis of the 12-SND's excess noise and linearity is presented, providing valuable information on the SND operation and on the potential for further scaling the dynamic range.

2. Device and experimental setup

A schematic diagram of the 12-SND is shown in Fig. 1(a). Twelve elements are connected in series and each of them consists of a section of superconducting nanowire, shunted with a parallel resistor R_p. The working principle of each element is similar to a standard SSPD [11]. Each element is biased with a current I_B, slightly lower than the critical current I_C, using a current source. When no photon arrives, the nanowire is in the superconducting state and the I_B flows through the nanowire. When a photon is absorbed, the photon energy suppresses the superconductivity in the nanowire and triggers the transition to the normal state. Since the resistance of the nanowire after photon absorption is much larger than the value of R_p, the I_B is diverted to the R_p and builds a voltage pulse across it. The photo-induced voltages of different elements are summed up in the readout resistor R_L (50Ω), producing a single output voltage pulse with a height proportional to the number of firing elements, and therefore to the number of detected photons.
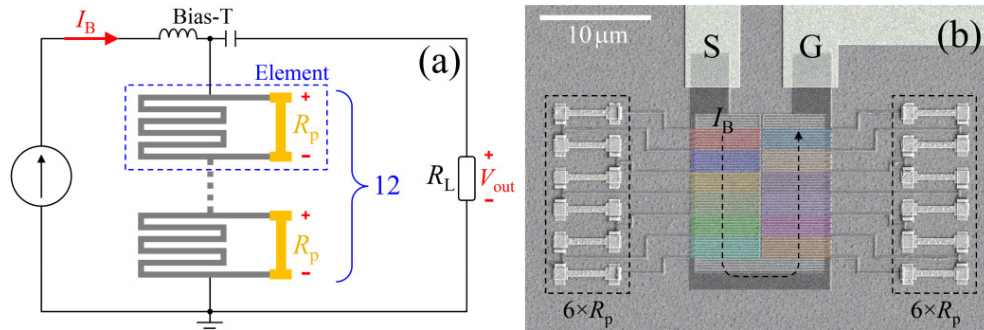

Fig. 1. (a) Schematic diagram of the 12-SND (not to scale). (b) SEM image of the 12-SND. The twelve active nanowires are highlighted in colors. The twelve R_ps, the signal (S) and ground (G) contact pads, and the direction of I_B are marked. The white scale bar in the upper-left corner of the image indicates a length of 10 μm.

A scanning electron microscope (SEM) image of the 12-SND is shown in Fig. 1(b). The fabrication process of the 12-SND is similar to that of the 4-SND as reported in [22]. After a 4.8 nm-thick NbN film was grown on a GaAs substrate by reactive DC-magnetron sputtering [24], four electron-beam lithography steps were taken to fabricate the 12-SND. First, the main electrical contact pads [Ti(10 nm)/Au(60 nm)] and alignment markers were fabricated by metal evaporation and lift-off using a polymethylmethacrylate (PMMA) stencil mask. The I_B flows through these contact pads [marked by S (signal) and G (ground) in Fig. 1(b)] into the device. Second, for each 12-SND, twenty-four smaller contact pads [Ti(5 nm)/Au(20 nm)] were made for the electrical contact of the twelve R_ps. Third, the NbN film was patterned by reactive ion etching using hydrogen silsesquioxane as an etch mask. The twelve active NbN nanowire sections [highlighted by different colors in Fig. 1(b)] were patterned in a 12 μm × 12 μm array with a filling factor of 40%. The nominal width of the NbN nanowires in the array is 100 nm, but the width was observed to vary from 75 nm to 105 nm in different pixels, depending on their position in the array, due to the proximity effect. In the last step, twelve R_ps [Ti(10 nm)/AuPd(50 nm)] were fabricated by lift-off using a PMMA stencil mask. The twelve R_ps locate on the sides of the nanowire array, each of them has a design value of 50 Ω and is connected to the array through the 250 nm-wide NbN nanowires.

In the experiment, the device was kept at a temperature of 1.2 K in a VeriCold cryostat, which consists of a Pulse Tube Cooler with an additional Joule-Thompson closed cycle. According to the current-voltage (IV) characterization of the 12-SND as shown in Fig. 2, the I_C of the device was 13.4 μA at 1.2 K. The typical relaxation-oscillation regime is not observed on the IV curve (solid red line) due to the presence of the twelve R_ps. When I_B exceeds I_C, the entire nanowire becomes resistive, so the measured resistance (dV_B/dI_B) equals

to the parallel equivalent of the nanowire's normal resistance and the value of $12 \times R_p$. Since the resistance of the normal nanowire is much larger than the value of $12 \times R_p$, the value of dV_B/dI_B can be approximated to be $12 \times R_p$ [22, 23]. As shown in Fig. 2, by calculating the reciprocal of the slope on the IV curve, the value of $12 \times R_p$ was determined to be ~542 Ω, and thus the average value of R_p was ~45.2 Ω, in good agreement with the design value of 50 Ω. The asymmetric shape of the IV curve in the normal region, which also showed hysteresis, was attributed to spurious reflections from the amplifier, which was connected to the device via the bias-T in the IV measurement and in the optical characterizations presented below.
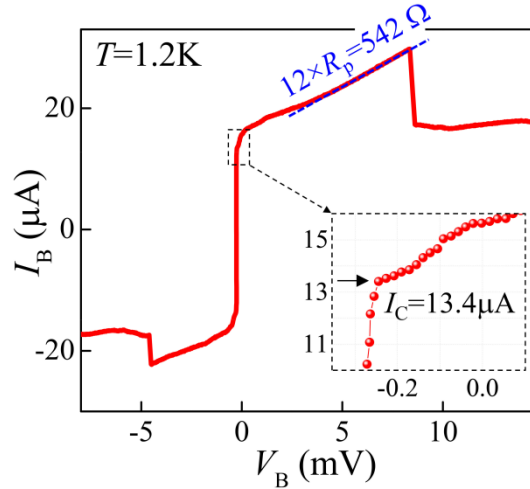

Fig. 2. IV characterization of the 12-SND at T = 1.2 K with the amplifier connected to the device. The value of $12 \times R_p$ is determined by calculating the reciprocal of the slope using a linear fit (dashed blue line). The inset presents an enlarged view on the IV curve. The I_C of the device was 13.4 μA.

A 1.31 μm diode laser with a pulse width (τ_p) of ~100 ps was used for the optical characterization in this work. The laser was triggered externally by a function generator with a repetition rate of 1 MHz. The 12-SND was illuminated by the laser through a polarization-maintaining single-mode lensed fiber mounted on a XYZ-piezo stage in the cryostat. The light spot was aligned to the center of the 12-SND and the lensed fiber tip was lifted up from its optimal focusing position to achieve a uniform illumination on the active area of the device. The full width at half maximum (FWHM) of the Gaussian spot was measured to be ~11.8 μm using the knife-edge method [25], which was performed by measuring the power of the light reflected back through the fiber tip while scanning the spot across the edge of the contact pads. Considering the size of the light spot, a ratio of ~33% of the light power from the fiber tip flowed into the 12 μm × 12 μm active area during the measurements. The optical response signal of the device was collected through the RF arm of the bias-T at room temperature, then amplified by a low-noise amplifier, and finally sent to either a 40-GHz sampling oscilloscope or a 350-MHz counter for analysis.

3. Characterization of multi-photon response

The optical characterization of the 12-SND was first performed with the 40-GHz sampling oscilloscope. The device was biased with an I_B of 13.0 μA. The sampling oscilloscope was synchronized with the laser's trigger signal and measured the amplified output voltage signals (V_{out}) from the device. A low-pass filter with a cutoff wavelength of 80 MHz was added in the readout circuit to improve the signal-to-noise ratio (SNR) of the output signals by removing high frequency noises. A MITEQ low-noise amplifier with 51 dB amplification, a 1.1 dB

noise figure, and a passband of from 0.5 to 500 MHz, was used in this measurement. The histograms of the output signals obtained in a power range of 0-64 nW are shown in Fig. 3 (All the light power values indicated in the following refer to the power exiting the lensed fiber). They were recorded within a 50 ps time window in order to make the DCR negligible. Thirteen distinct output levels corresponding to the detections of 0-12 photons were obtained, showing a large dynamic range of the 12-SND.
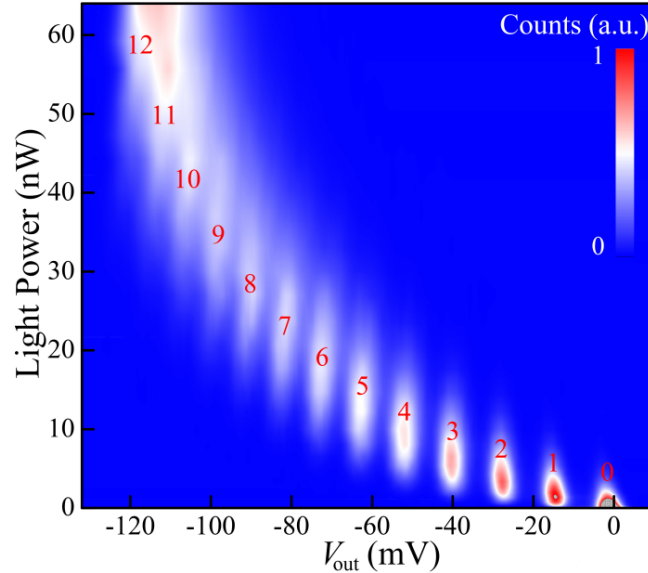

Fig. 3. The histograms of the output signals obtained in a light power range of 0-64 nW. Thirteen distinct output levels corresponding to the detections of 0-12 photons (marked by red numbers) were obtained. The device was biased with an I_B of 13.0 μA.

To further confirm the PNR functionality of the 12-SND, we studied the count rate (CR) dependence on the light power, using the 350-MHz counter. As shown in Fig. 4, the CR was measured as a function of the input light power by setting different trigger levels of the counter (the DCR was subtracted from the data). The trigger level was chosen between the nth and the $(n + 1)$th output levels in Fig. 3 so that the counter only recorded the '≥n-photon' responses. According to [22], when the light power is low so that $\eta\bar{\mu} \ll 1$ ($\bar{\mu}$ is the average photon number per light pulse incident on the active area of the device and η is the device quantum efficiency obtained with respect to $\bar{\mu}$), the CR should be approximately proportional to the value of $(\eta\bar{\mu})^n$ and thus proportional to the nth-order of the light power. This is confirmed by our results as shown in Fig. 4. In the power range of up to 4 nW, which approximately corresponds to $\eta\bar{\mu} < 1$, the slope of the curves agrees with the value of 1, 2, $\cdots$, and 7 for the corresponding photon regimes.
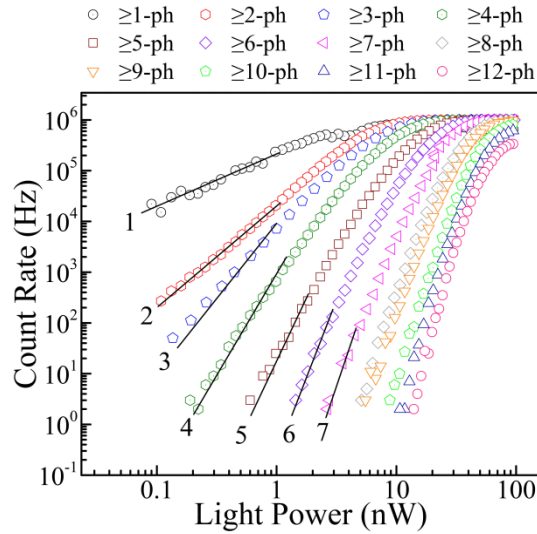
Fig. 4. The measured CR plotted as a function of the light power by setting different trigger levels of the counter, corresponding to the detections of '≥n-photons' (n = 1-12). The slopes of the curves at lower powers agree well with the $\left(\eta\overline{\mu}\right)^{n}$ dependence (indicated by solid black lines), providing a proof for the 12-SND's PNR functionality.

After aligning the light's polarization direction parallel to the nanowires [26], the device quantum efficiency η was measured by measuring the CR with the counter whose trigger level is set between the 0th and 1st output levels. As shown in Fig. 5, the value of η is plotted as a function of I_B, reaching a maximum value of ~0.17% at I_B = 13.2 μA. The low efficiency of the present device is due to the low optical absorptance (in the order of few percent [24]) of NbN nanowires on GaAs substrates, and also due to the inhomogeneities of the NbN nanowires which effectively reduced the device's active area [27, 28]. The efficiency can be improved by changing the substrate [26], integrating a microcavity [24, 29] or an optical waveguide [23], and by optimizing the quality of the NbN film and the fabrication process.

The temporal response of the 12-SND was also characterized. As shown in the inset of Fig. 5, the photoresponse pulse for the 12-photon detection was recorded by the 40-GHz sampling oscilloscope. A chain of two Mini-circuit low noise amplifiers, both of which had 13 dB amplification, 2.6 dB noise figure, and 0.02-3 GHz passband, was used in this measurement for a better temporal resolution. The 80 MHz low-pass filter was removed from the readout circuit in this case. As shown in the inset of Fig. 5, we calculated the temporal photoresponse (dashed blue line) for the 12-photon detection based on the electro-thermal model reported in [21, 30] using the parameters of the present 12-SND. After applying a band-pass filter (0.02-3 GHz, corresponding to the passband of the amplifiers) to the dashed blue line, the result (solid red line) presents a good agreement with the measurement, giving a fall time τ_{fall} of ~11.3 ns, which enables a maximum repetition rate of ~30 MHz. The system time jitter was measured at the leading edge of the photoresponse pulse to be ~89 ps, including the jitter of the 12-SND, of the laser and of the amplifiers. We note that with the present 12-SND, a trade-off exists between the temporal performance and the SNR in the PNR operation, depending on whether the low-pass filter is used in the circuit. However, this will not intrinsically limit the performance of the SNDs. We can increase the SNR by using cryogenic pre-amplifiers and by improving the uniformity of the device, releasing the need for a low-pass filter.
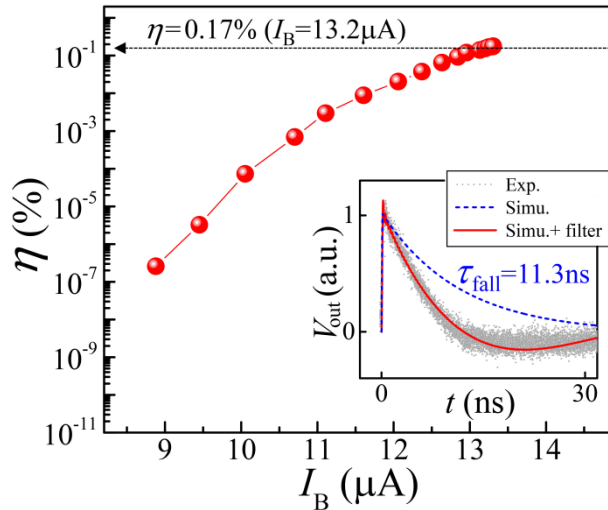
Fig. 5. Device quantum efficiency as a function of I_B, reaching a maximum value of ~0.17% at $I_B = 13.2$ μA. Inset: photoresponse pulse for the 12-photon detection recorded by the 40-GHz sampling oscilloscope. The dashed blue line is the calculated photoresponse pulse for the 12-photon detection event, giving a fall time τ_{fall} of ~11.3 ns. After applying a band-pass filter (0.02-3 GHz, corresponding to the passband of the amplifiers) to the simulation, the result (solid red line) shows a good agreement with the measurement.

4. Photon number statistics

In order to assess the capability of the 12-SND to measure the photon number statistics, we compare the photon number distribution measured in Fig. 3 with the expected distribution of a Poissonian source. The histograms of Fig. 3 at different input light powers were fitted by a sum of Gaussian peaks, using the amplitude, position and width of the peaks as fitting parameters for each power. For example, Fig. 6(a) and 6(b) show two profiles of Fig. 3 at two different powers of 5.33 nW and 20.59 nW together with their fittings, corresponding to the detections of $n = 0$-6 and $n = 3$-10 photons, respectively.
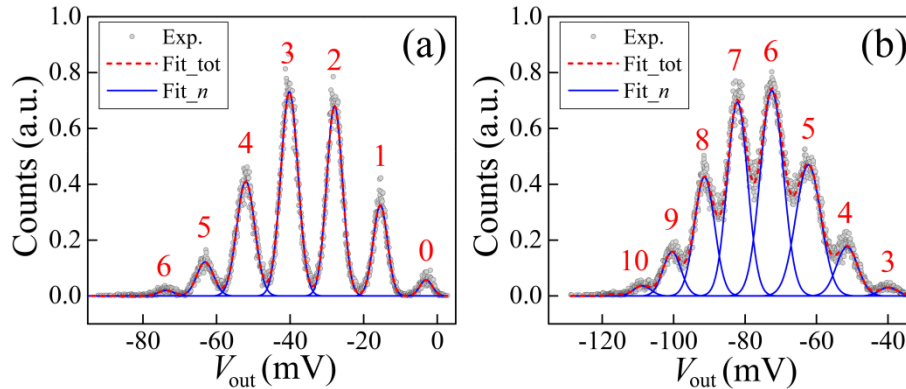

Fig. 6. Two profiles (grey dots) of Fig. 3 at two different light powers of 5.33 nW (a) and 20.59 nW (b). They are fitted using a sum of Gaussian peaks, corresponding to the detections of $n = 0$-6 (a) and $n = 3$-10 (b) photons, respectively. The single Gaussian fits (Fit_n) are shown as solid blue lines and their sum (Fit_tot) is depicted as a dashed red line.

The normalized area of each fitting Gaussian peak in the nth output level corresponds to the probability P of detecting n photons. This detection probability distribution deviates from the simple Poissonian statistics of the light source due to the possibility that several photons are absorbed in the same element, which is intrinsic to all multiplexed PNR detectors with a

finite number of elements. According to Fitch *et al.* [5], for a coherent laser source uniformly incident on an array of N detection elements, the probability P of detecting n photons can be written as,

$$P_\eta^N\left(n|\bar{\mu}\right)=\sum_{m=n}^{\infty}\frac{N!}{n!\left(N-n\right)!}\frac{\left(\eta\bar{\mu}\right)^m e^{-\eta\bar{\mu}}}{m!}\times\sum_{j=0}^{n}\left(-1\right)^j\frac{n!}{j!\left(n-j\right)!}\left[1-\eta+\frac{\left(n-j\right)\eta}{N}\right]^m \quad (1)$$

The value of $P_\eta^N\left(n|\bar{\mu}\right)$ obtained at different light powers in the experiment are extracted from Fig. 3 and are presented in Fig. 7 as black dots. The measured value of $P_\eta^N\left(n|\bar{\mu}\right)$ was then fitted by calculations (red stars in Fig. 7) based on Eq. (1) using a single fitting parameter η for each power. A good agreement between the measurements and the calculations is achieved over the entire power range. The fitted values of η are lower than the value reported in Fig. 5 for the I_B of 13.0 μA, since in this case the polarization was not aligned along the wires.

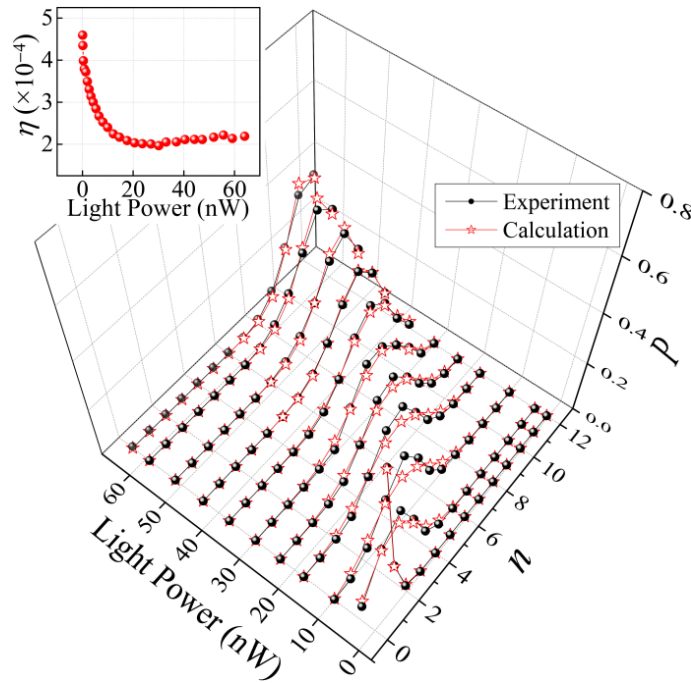Fig. 7. The value of $P_\eta^N\left(n|\bar{\mu}\right)$ (black dots) at different light powers extracted from Fig. 3 and the fitting (red stars) based on Eq. (1) using a single fitting parameter η. Inset: the value of η obtained from the fitting is plotted as a function of the light power.

We notice that when the light power increases, η first decreases and then maintains the minimum value at higher powers, as shown in the inset of Fig. 7. We attribute this observation to the non-uniformity of the elements' efficiency of the 12-SND. With low powers (low $\bar{\mu}$), only the most efficient elements fire so we see the highest value of η in the low power range; when $\bar{\mu}$ increases, the less efficient elements also participate in the detection so that the average efficiency drops. There are three possible reasons for the non-uniformity of the elements' efficiency. The first is due to the fact that the illumination was not perfectly uniform on the twelve elements. The illumination uniformity can be improved by either further increasing the Gaussian spot size or changing the spatial arrangement of the elements [31]. The second is due to the imperfections in the nanowires from the fabrication.

Particularly the observed variation in wire width results in a variation of the efficiency among the different elements. This can be avoided by further optimizing the fabrication process. The third reason is due to the decreasing of the bias current in the unfiring elements (I_{uf}) when other elements fired. As shown in Fig. 8(a), we calculated the value of I_{uf} as a function of time based on the electro-thermal model [21, 30]. The value of I_{uf} obviously decreases in the cases of detecting $n = 1$-11 photons due to the partial redistribution of the I_B to the 50 Ω load [21]. The inset provides an enlarged view of the I_{uf}, where the temporal profile of the incident pulse ($\tau_p = 100$ ps) is also indicated. Since the value of I_{uf} decreases in the time window where the detection events take place, the efficiency of the unfiring elements will decrease. Although this is not desirable for PNR detection, it can be avoided by using a much shorter light pulse or using a larger load resistance (e.g. a pre-amplifier with high input impedance [21]). As an example, the calculation of I_{uf} for $R_L = 1$ MΩ was performed and is presented in Fig. 8(b), keeping the other parameters unchanged. In this case, the value of I_{uf} remains constant so the efficiency of the unfiring elements will not decrease as a function of time.
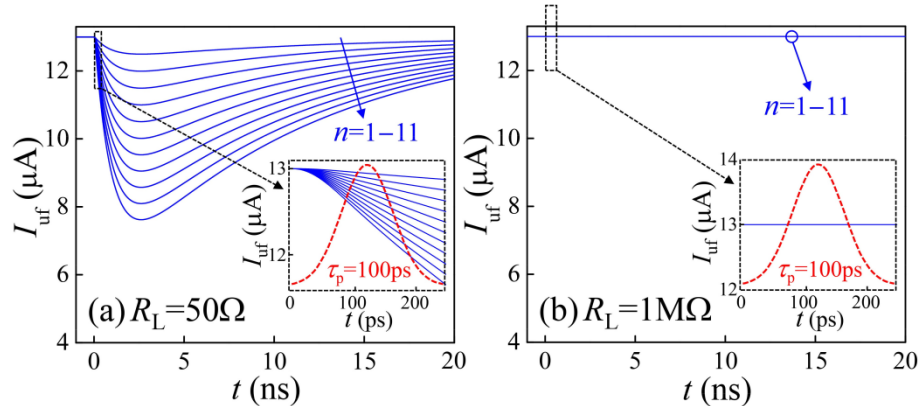

Fig. 8. The calculated value of I_{uf} (solid blue lines) as a function of time in the cases of detecting $n = 1$-11 photons, for $R_L = 50$ Ω (a) and $R_L = 1$ MΩ (b), respectively. The inset provides an enlarged view of I_{uf} where the temporal profile of the incident pulse ($\tau_p = 100$ ps, dashed red line) is also indicated.

5. Detection linearity of the 12-SND

The PNR capability of the 12-SND is determined by the linearity and by the detection noise. A high linearity and a low noise are preferable for the PNR detection as they ensure a large dynamic range. In the following we focus on the linearity of the 12-SND based on the data of Fig. 3.

We first investigate the dependence of the height of the n-photon output levels on the light power. The height (H) of the output voltage levels, defined as the height of the fitting Gaussian peaks extracted from Fig. 3, is plotted as a function of light power in the range of 1.95-30.11 nW for $n = 0$-11 in Fig. 9(a) (H of the $n = 12$ peak is not shown here since the $n = 12$ peak is only observed when the power is larger than 30.11 nW, where the fitting becomes unreliable due to the noise at high powers). As shown in Fig. 9(a), for each n, the value of H is almost independent of the power when the power is low; as the power increases, the value of H starts to slightly decrease. To visualize the small amount of the change of H, we define ΔH as the value of H at different powers subtracted by the value of H at the lowest power for the same n as shown in Fig. 9(a). The value of ΔH is plotted in Fig. 9(b) as a function of the power for different n, showing a decrease of H by up to a few percent as the power increases. Since the value of ΔH is small, the increase of light power does not have a significant influence on the detection linearity.

It is interesting to understand why H decreases as the power increases. Indeed we have also observed that the height of the photoresponse pulses from a standard SSPD decreases with the light power. A similar observation was reported in [17]. We attribute this phenomenon to the variation of the film's local characteristics or geometry (i.e. width and thickness) along the nanowires. In general, the narrower sections of the wire have higher current density and are more easily triggered by single photons. Thus, at low light powers, the output pulse height will be determined by the normal resistance of these narrower sections. When the power increases, the wider sections of the wire will be triggered by multi-photons, contributing to the photocounts. Since the wider sections have a lower normal resistance, the height of the photoresponse pulses will decrease at higher powers, and the distribution of the height will be broadened [as shown below in Fig. 11(a)].
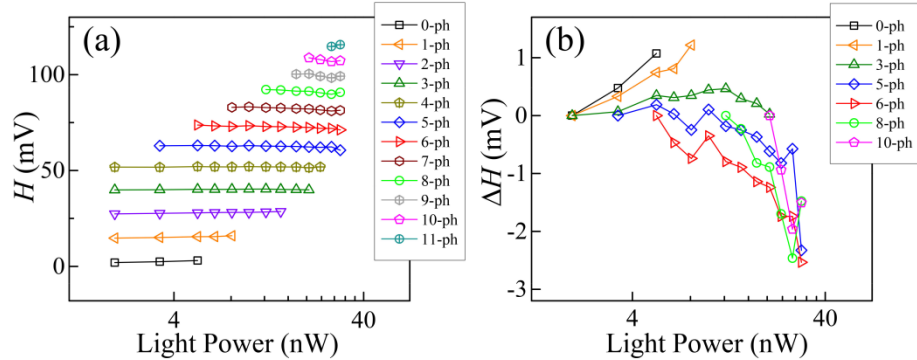

Fig. 9. (a) The value of H extracted from Fig. 3 plotted as a function of light power for different n. (b) The value of ΔH, defined as the value of H at different powers subtracted by the value of H at the lowest power for the same n, as a function of power for a few n in the 0-10 range.

We then investigate the dependence of H on n. Since the change of H is relatively small as the power changes, we calculated the value of H averaged for different powers (namely $\bar{H}$) according to Fig. 9(a), and plotted it as a function of n in Fig. 10(a). A power-law fit to $\bar{H}$, defined as $\bar{H} = A \cdot n^{\alpha}$ (A and α are fitting parameters), is also plotted, giving $\alpha = 0.81$. The difference between the value of $\bar{H}(n)$ and $\bar{H}(n-1)$, defined as $\Delta \bar{H} = \bar{H}(n) - \bar{H}(n-1)$, is plotted as a function of n in the inset of Fig. 10(a), showing that the value of $\bar{H}$ increases nonlinearly with n. We calculated the value of V_{out} as a function of time for $n = 1\text{-}12$ using the electro-thermal model [21, 30] and plotted the results in the inset of Fig. 10(b). The calculated value of H, i.e. the maximum value of V_{out} of these pulses, is extracted and plotted as a function of n in the main panel of Fig. 10(b). By fitting the calculated value of H, we obtained an α of 0.98, showing a better linearity than that in the experiment.

We attribute the difference of the α values between the experiment and the simulation to the inhomogeneities among different elements, e.g. variation in the wire's cross section between different elements. In principle, the elements with narrower wires have higher efficiency, so with small n only they will contribute to the readout voltage pulse; the wider elements will participate in detections as n increases. Since the voltage pulse produced by the wider elements is lower than that of the narrower elements, the height of total voltage pulse scales nonlinearly with the n. As shown in the discussions below, this variation in the voltage amplitudes of different elements has major consequences also in the noise.
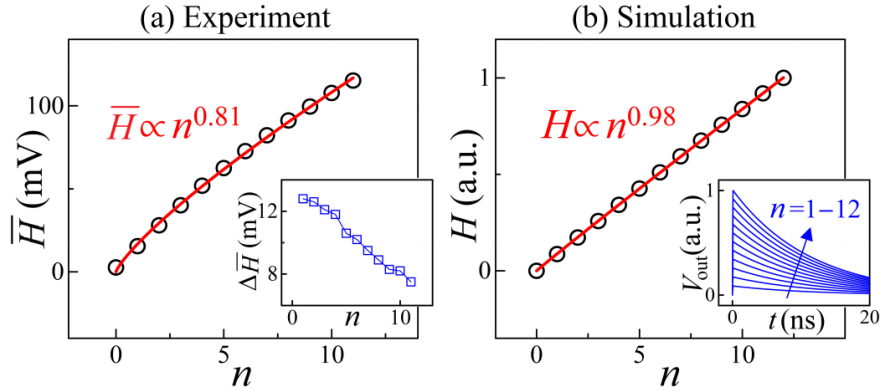
Fig. 10. (a) The value of H averaged for different powers (namely $\overline{H}$) plotted as a function of n (black dots). A power-law fit (red line) to $\overline{H}$, defined as $\overline{H} = A \cdot n^{\alpha}$, is also plotted, giving $\alpha = 0.81$. Inset of (a): The value of $\Delta\overline{H}$, defined as $\Delta\overline{H} = \overline{H}(n) - \overline{H}(n-1)$, is plotted as a function of n. Inset of (b): the calculated V_{out} plotted as a function of time for n = 1-12 using the electro-thermal model [21, 30]. Main panel of (b): the value of H (black dots) extracted from the inset of (b), plotted as a function of n together with a power-law fit (red line), giving $\alpha = 0.98$.

6. Detection noise of the 12-SND

We then investigate the dependence of the detection noise on the light power and on n. The noise V_N on the output levels, defined as the FWHM of the fitting Gaussian peak, is extracted from Fig. 3 for n = 0-11 in the power range of 1.95-30.11 nW.
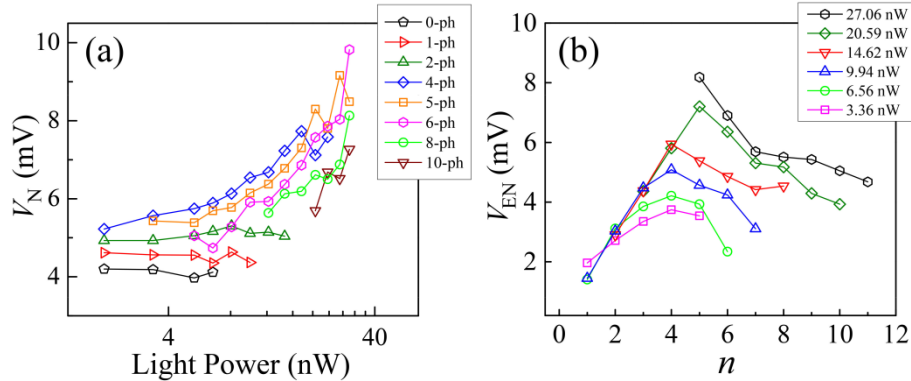

Fig. 11. (a) The value of V_N plotted as a function of the light power for a few n in the 0-10 range. (b) The value of V_{EN} plotted as a function of n for different light powers.

On the one hand, as shown in Fig. 11(a), the value of V_N for the nth detection increases with the light power. This phenomenon is related to the observation that the value of H decreases as the light power increases as shown in Fig. 9. As discussed above, it can be attributed to the triggering of wire's wider sections by multi-photon events at high powers, which in principle results in a smaller pulse height and at the same time a broadened distribution of height. Since this type of noise critically depends on the uniformity of the film along the wire, it can be suppressed by optimizing the processes of film deposition and of device fabrication.

On the other hand, the excess noise V_{EN}, defined as $V_{EN} = \sqrt{V_N^2(n) - V_N^2(n=0)}$, is plotted as a function of n at fixed light powers as shown in Fig. 11(b). Interestingly, for all powers, the value of V_{EN} first increases with n, reaching a maximum for $n \approx$ 4-6, depending on the

power, then decreases. This dependence indicates a surprising suppression of the excess noise, which is key to the measurement of large photon numbers.

We attribute the excess noise to three possible origins. The first is due to the thermal noise of the amplifier. The thermal noise produced by the equivalent noise current generator of the amplifier depends on the detector's impedance, which dynamically varies during the detection events and depends on the number of absorbed photons [22].

The second source of noise is due to the accumulation of the intrinsic noises from each of the n detection events. As discussed above, the intrinsic noise from each element is related to the inhomogeneities of the nanowires and increases with the light power. With a fixed light power, the noises in distinct wires are uncorrelated; the variance of their sum scales as n and their total contribution to V_{EN} is expected to scale as $\sqrt{n}$.

The third source of noise results from the variation of the height of the output pulses produced by different elements, which is due to the variation of the nanowire's normal resistance in different elements (the variation of R_p may also change the pulse height, but it is not considered in the following discussion for simplicity). Based on our explanation to Fig. 10(a), we assume at low powers, only the most efficient element, which has the narrowest wire and produces the highest photoresponse pulse, participates in the detection, and at high powers, the least efficient element starts to participate. In this case, according to the inset of Fig. 10(a), the most efficient element produces a pulse height of ~12.8 mV; likewise, the element with the lowest efficiency produces a pulse height of ~7.5 mV, and the other elements produce pulse heights distributed around a mean value of ~10 mV. We further assume that variation of the output pulse height of different elements is the only noise source for Fig. 11(b), so the pulse height distribution has a width of ~2 mV according to Fig. 11(b) as $n = 1$.
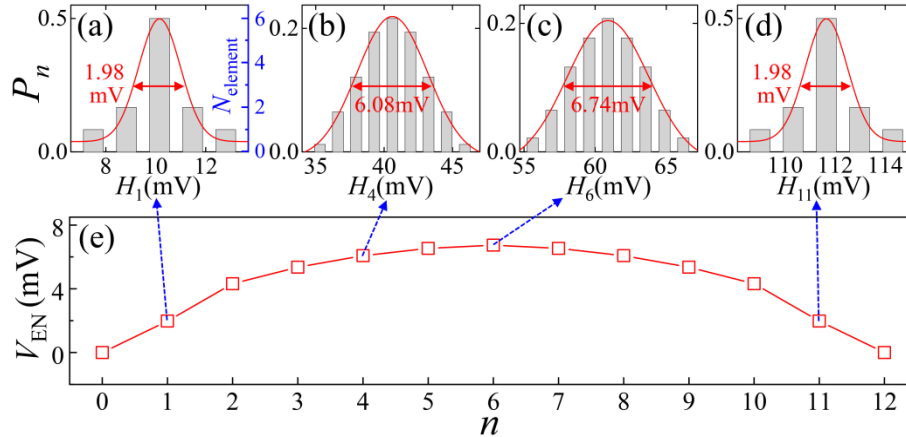

Fig. 12. The distribution of $N_{element}$ (H_1) and the corresponding distribution of P_1 (H_1) are shown as histogram (grey bars) in (a) to the right and to the left axis, respectively. The distribution of P_n (H_n) for n = 0-12 is calculated based on P_1 (H_1) assuming a uniform distribution of the elements' efficiency. The examples for n = 4, 6 and 11 are plotted as histograms (grey bars) in (b), (c) and (d), respectively. Each P_n (H_n) distribution is fitted by a Gaussian peak (red lines). The FWHM of the fitting Gaussian peak, which represents V_{EN}, is plotted as a function of n in (e) for n = 0-12. The V_{EN} for the examples of n = 1, 4, 6 and 11 is marked in (a)-(d), respectively.

Using the above assumptions, we calculate the expected excess noise for the n-photon detection. We assume an arbitrary distribution $N_{element}(H_1)$ of the number of elements producing a peak height H_1 for the one-photon detection (n = 1) [grey bars in Fig. 12(a), right axis], chosen so that the highest and the least pulse height have values of 12.8 mV and 7.5 mV, and the width is ~2 mV [using a Gaussian fit (red line)]. Based on the distribution of $N_{element}(H_1)$, we are able to calculate the distribution of P_n (H_n) considering a uniform

distribution of the elements' efficiency, where P_n is the probability of detecting a pulse with the height of H_n in the n-photon detection event (n = 0-12). When $n = 0$, $H_0 = 0$ and the width of the distribution equals zero. When $n = 1$, the distribution of P_1 (H_1) [Fig. 12(a), left axis] reproduces the distribution of $N_{element}(H_1)$. When $n>1$, each n-photon detection is a combination of n one-photon detections corresponding to any n of the twelve elements. The value of P_n (H_n) equals to the sum of the probabilities for all the possible combinations which produce H_n. The calculation of P_n (H_n) for n = 0-12 has been done based on the above rules. Four examples for n = 1, 4, 6 and 11 are plotted as histograms (grey bars) in Figs. 12(a)-12(d), respectively. Each calculated P_n (H_n) distribution is fitted by a Gaussian peak [red lines in Figs. 12(a)-12(d)]. The FWHM of the fitting Gaussian peak, which represents the calculated V_{EN}, is plotted as a function of n in Fig. 12(e). Interestingly, the shape of the P_n (H_n) distribution for the n-photon event is identical to that of the (12-n)-photon event. For instance, the one-photon event as shown in Fig. 12(a) reproduces the distribution of the eleven-photon event as shown in Fig. 12(d), despite of the shift of the H_n values. It is also interesting to see that the excess noise drops to zero when n = 12 as shown in Fig. 12(e). Indeed, if all the twelve elements are triggered, only a single value of H_{12} is possible, so no excess noise appears for n = 12. The calculated n-dependence of V_{EN} agrees with the experimental data. The calculation [Fig. 12(e)] gives the highest noise at n = 6, while in the experiment [Fig. 11(b)] the highest noises take place in the range of n = 4-6. The agreement clearly indicates that the statistical distribution of the nanowire's normal resistance plays an important role in the observed excess noise.

7. PNR capability of the 12-SND

Based on the above discussions on the linearity and the detection noise of the 12-SND, we take the ratio of $\Delta H/V_N$ as a measure of the 12-SND's PNR capability. Indeed, the fidelity of discriminating an n-photon detection from (n-1) or (n + 1) directly depends on the ratio between the peak spacing and the peak width, i.e. the noise. For example, for equally spaced Gaussian peaks with constant width, the probability of correctly measuring an n-photon peak with an optimal discrimination threshold [32] is 76.09%, 98.15% and 99.96% for $\Delta H/V_N$ = 1, 2 and 3, respectively. The measured ratio of $\Delta H/V_N$ [calculated based on the data of Fig. 9(a) and Fig. 11(a)] is plotted it in Fig. 13 as a function of n for different powers.
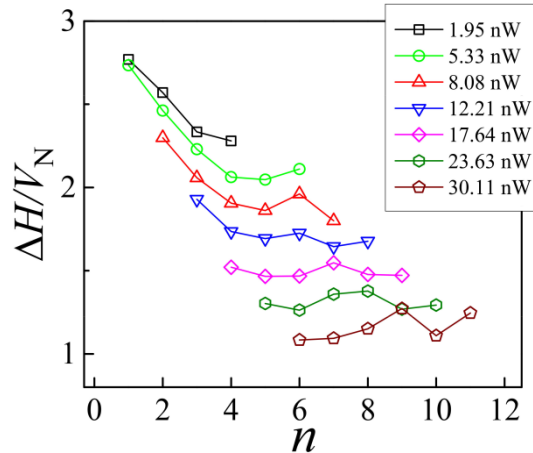

Fig. 13. The ratio of $\Delta H/V_N$ plotted as a function of n for different powers.

As shown in Fig. 13, the increase of light power results in a decrease of the PNR capability, this is mainly due to the fact that the noise, i.e. V_N, is increased as the power increases. Secondly, the PNR capability decreases as n increases when n is small and then

tends to stop decreasing when n becomes larger. This is due to the saturation of V_{EN} as discussed above, showing a potential of scaling to larger dynamic range. The ratio of $\Delta H / V_N$ may be greatly increased by using a cryogenic high-impedance pre-amplifier to boost the ΔH [21]. We note that the above discussion does not include the fidelity limitations imposed by the limited efficiency and number of wires, which has been previously addressed in the literature [31].

8. Conclusions

In summary, we presented a PNR detector based on a series connection of twelve superconducting NbN nanowires. This detector, named as 12-SND, provides a single output pulse with a height proportional to detected photon numbers. The 12-SND is able to resolve up to twelve photons, providing a record dynamic range among the existing fast telecom-wavelength PNR detectors. The 1/e decay time of the device was ~11.3 ns, enabling a repetition rate of ~30 MHz. The system jitter was measured to be ~89 ps. The correct PNR operation was verified by studying the count rate and the distribution of the output levels as a function of the photon number and of the light power. The noise analysis reveals a surprising suppression of the excess noise at high photon numbers, which is attributed to the statistical distribution in the normal resistance of the nanowires. This indicates an excellent potential of the SND of scaling to even higher photon numbers, especially if the uniformity of the nanowire and of the parallel resistances is improved. Moreover, the combination of the SND with a cryogenic pre-amplifier with high input impedance will further improve the performance of the SNDs [21]. By using the pre-amplifier, the bias current in the unfiring elements will not decrease, resulting in higher output signals, improved discrimination of the voltage levels, better linearity, and higher speed.

Acknowledgments